Inorganic Chemistry

Article

pubs.acs.org/IC

One Pot, Two Phases: Individual Orthorhombic and Face-Centered Cubic $ZnSnO_3$ Obtained Synchronously in One Solution

Ying Wang,[†] Peng Gao,*[,†] Di Bao,[†] Longqiang Wang,[†] Yujin Chen,*[,‡] Xiaoming Zhou,[†] Piaoping Yang,*[,†] Shuchao Sun,[†] and Milin Zhang[†]

[†]College of Materials Science and Chemical Engineering and [‡]College of Science, Harbin Engineering University, Harbin, Heilongjiang 150001, P. R. China

Supporting Information

ABSTRACT: Many modern technologies rely on the functional materials that are subject to their phase purity. The topic of obtaining pure crystals from the concomitant allotropes is ever before the eyes of numerous researchers. Here we adopt a template-inducing route and obtain the isolated allotropes located in the appointed regions in the same reaction system. As a typical example, well-defined individual face-centered cubic and orthorhombic $ZnSnO_3$ crystals were successfully synthesized assisted by a ZnO inducing template or without it in an identical solution, respectively. And the different growing mechanisms of the $ZnSnO_3$ allotropes were also proposed, which takes a pivotal step toward the realization of allotropes dividing. Moreover, the two individual pure-phased $ZnSnO_3$ allotropes obtained in one reaction system exhibit porous microspherical morphologies constructed by the tiny nanograins, resulting in their high sensitivities to ethanol with fast response and recovery and good selectivity and stability.

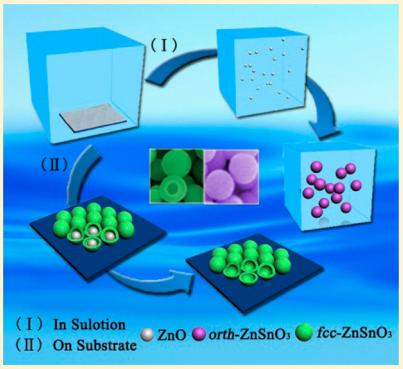

INTRODUCTION

Allotropes are the special forms of chemical elements that exhibit the different atoms' arrangement and crystal structure. However, in many materials it is an inevitable phenomenon that the concomitant allotropes form synchronously in the identical reaction system.[1,2] Currently there is substantial research effort dedicated to understanding allotropes and to exploring purification techniques with convenient and accurate operation.[3,4] The exploration is very important not only to inorganic chemistry but also to the entire field of chemistry and material sciences, which has become a challenging problem in related researches.[5−8] Almost all the materials, such as metals, biomaterials, inorganic compounds, carbon materials, and polymers, have allotrope structures that need the following laborious purification assisted by temperature, stress, pH, and/or doping controlling.[9−17] For example, in the production of carbon materials, such as carbon nanotubes and C_{60}, significant amounts of carbonaceous impurities, including amorphous carbon and carbon nanoparticles, are generated, and the products often need to be purified rigorously using metal catalyst and column chromatography, respectively, which limits their large-scale applications and in-depth research;[18,19] Vaterite has been found in biological settings and proved as an important precursor in several carbonate-forming systems; however, up to now its crystal structure is still elusive for almost a century because of the difficulties in obtaining its pure single crystal from its two coexisting allotropes;[20] the high-pressure allotropes of rare-earth metals, such as lanthanum, cerium, praseodymium, and neodymium, have important applications in superconducting and fluorescent material fields, but their formation mechanism is still unclear.[21,22] Between enantiomers of a chiral herbicide, there is a drastic difference in herbicidal activity and nontarget toxicity. The separation of the enantiomers of chiral herbicides is difficult, and they are usually separated and analyzed by chromatographic methods such as high-performance liquid chromatography (HPLC) and gas chromatography (GC), which increase their production costs and limit their commercialized applications.[23,24] Now, though many purification methods have been conducted to isolate the target particles from their allotrope mixtures, additional chemical treatment, extra energy input, and the assistance of other equipment absolutely led to an order of magnitude increase in the cost of the purified material. Therefore, the headstream of solving the allotrope puzzle is to find a controllable method to induce them individually to be located in their formations, and developments are unavoidable.

In general, the formation of crystalline material involves two major processes according to the La Mer-mechanism: nucleation and growth.[25−27] Nucleation occurs at the very beginning of a synthesis, during which precursor molecules are reduced to reactants, elemental atoms/molecules that will serve as building blocks for the formation of crystals. Once the concentration of reactants reaches the point of supersaturation, small clusters will appear through aggregation of these reactants. They will further evolve into seeds and serve as the active sites for the atoms/molecules product. Continuous growth of the seeds results in the generation of crystals as final

Received: June 15, 2014
Published: November 13, 2014

products. Even small variations inflicted on the two processes often lead to large changes in crystal structure and morphology. So a suitable synthetic condition of nucleation and growth selected will induce the formation of specific crystalline phase. It is well-known that the template could affect the crystal growth process in a certain extent, and now a variety of templates have been proposed to get special crystal phase, orientation, size, and morphology.[28−31] For example, TiO_2-based nanotubes have been successfully prepared on a titanium substrate covered with TiO_2 nanoparticle seeds, and it is found that neither the composition nor the structure of the as-synthesized nanotubes agree with that expected from tubes made of normal TiO_2 crystals with either anatase or rutile phases.[32] Through an amorphous-to-crystalline transitions assisted by the specially designed structural templates with integrated nucleation sites, calcite structured $CaCO_3$ films have been successfully prepared.[33] So the template method can affect the crystal growth process and even result in the special crystal phase that is of potential application in metal oxide synthesis with enhanced control on the phases. In the present work, we attempt to introduce a template into a reaction system, which will induce a special crystal phase in the allotropes formed synchronously in the system to grow preferentially on it. This may provide a new method for dividing allotropes through controlling the material's initial nucleation and growth process when their formation is unavoidable.

As an excellent gas-sensitive material, $ZnSnO_3$ has orthorhombic (*orth*) and face-centered cubic (*fcc*) phases. Recently, the two phases of $ZnSnO_3$ materials have been synthesized by different routes, such as template route, hydrothermal synthesis, and coprecipitation method.[34−36] In the above literatures, it is found that the atmosphere conditions affected the material's nucleation and growth process greatly, resulting in the formation of their different phases. Experimentally, a mixture containing a small quantity of ZnO powder, some urea, and potassium stannate trihydrate were hydrothermally treated at 120 °C for 3 h by us. It was found that *orth*- and *fcc*-$ZnSnO_3$ mixtures were obtained (Supporting Information, Figure S1). Considering the template function of ZnO precursor for $ZnSnO_3$, which has been demontrated in our previous work,[34] an interesting ZnO template-inducing method is proposed by us to obtain the isolated allotropes located in the appointed regions in the same reaction system. In the above method through a free nucleation process in the reaction solution containing K_2SnO_3 and ZnO molecules, pure *orth*-$ZnSnO_3$ deposit is obtained. Meanwhile, pure *fcc*-$ZnSnO_3$ product growing on the ZnO inducing template is also gathered, which locates on the Zn substrate. These $ZnSnO_3$ allotrope products formed in the specific regions separate naturally, and this process does not require any extra energy input, additional chemical treatment, or the assistance of any other equipment. Therefore, this facile and cost-effective approach opens a new window to resolving the separation puzzle hovering on the crystalline concomitant allotropes, which is of great industrial interest.[37]

EXPERIMENTAL SECTION

Synthesis of ZnO Precursors. All the reagents were analytic grade reagents and used without further purification. In a typical experiment, first, a piece of pure zinc foil ($0.02 \times 1 \times 1$ cm^3) and 30 mL of sodium dioctyl sulfosuccinate solution ($C_{20}H_{37}NaO_7S$, OT, 1.50 g/L) were transferred into a 50 mL Teflon-lined stainless steel autoclave and heated to 100 °C for 2 h. After cooling to room temperature, the foil was washed with distilled water and absolute ethanol several times.

Synthesis and Characterization of $ZnSnO_3$ Microspheres. $ZnSnO_3$ microspheres were prepared via a facile and low-cost solution synthesis process. For the solution chemical synthesis of $ZnSnO_3$ microspheres, 0.75 g of urea ($CO(NH_2)_2$) and 0.25 g of potassium stannate trihydrate ($K_2SnO_3{\cdot}3H_2O$, 95%) were added into the 30 mL of water−alcohol (38 vol % alcohol) solvent. After stirring for 5−10 min, the formed suspension was transferred into a 50 mL Teflon-lined stainless steel autoclave with the foil first step and heated to 120 °C for 3 h in an electric oven. After cooling to room temperature, the obtained foil and precipitates were washed several times with absolute ethanol and distilled water, respectively. Then the microspheres were dried in the air at 60 °C for 6 h. The crystal structure and morphology of the as-prepared products were characterized by X-ray diffraction (XRD, D/MAX2500, Cu Kα radiation, λ = 1.54 Å), scanning electron microscopy (SEM, JEOL JSM6700F), transmission electron microscopy (TEM), high-resolution transmission electron microscopy (HRTEM), and selected-area electron diffraction (SAED, JEOL 2010). Surface area was measured via the BET method of N_2 adsorption isotherms performed at 77 K on a Micromeritics Instrument Corporation TriStar II 3020 surface area and porosity analyzer. The room-temperature photoluminescence (PL) spectrum was measured using a spectrophotometer (Jobin Yvon Fluorolog3−221) with a Xe lamp (450 W) as excitation source at the excitation wavelength of 270 nm. The resistivity of the material was determined as a function of the deposition parameters using the four-point probe method. The optical absorption properties of the products were measured by a UV−vis spectrometer (UV-3600, Shimadzu).

Fabrication and Measurement of Gas Sensor. The fabrication process of the sensors using these nanostructures was described elsewhere.[38,39] Briefly, the sensing materials were dispersed in ethanol, and a drop was spun on a ceramic tube between Pt electrodes to form a thin film (~tens of nanometers). A Ni−Cr heating wire in the ceramic tube was used to control the working temperature. The structure of the sensor is shown in Figure 1a. The schematic

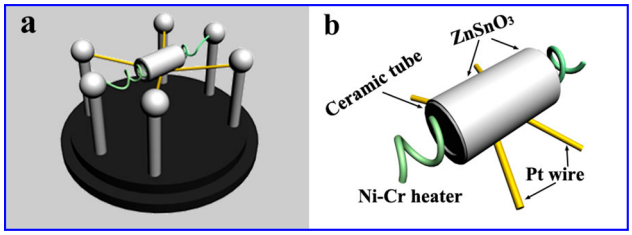

Figure 1. (a) The photograph of indirect-heated gas sensor. (b) The schematic representation of indirect-heated gas sensor.

representation of indirect-heated gas sensor is shown in Figure 1b. The sensitivity (S) of the product in this paper is defined as $S = R_a/R_g$, where R_a is the sensor resistance in air, and R_g is the resistance in the target−air mixed gas. The response and recovery time are defined as the time taken by the sensor to achieve 90% of the total resistance change in the case of adsorption and desorption, respectively.

RESULTS AND DISCUSSION

Structural and Morphological Characteristics of *fcc*-$ZnSnO_3$ Hollow Microspheres on the Substrate. After the foil covered with ZnO (Supporting Information, Figure S2) is immersed into the solution containing K_2SnO_3 and $CO(NH_2)_2$ and heated at 120 °C for 3 h, $ZnSnO_3$ nanoparticles are obtained successfully on the foil. The detailed composition, purity, and crystal structure of the product is first investigated by XRD measurements, as shown in Figure 2a. All the diffraction peaks except those belonging to Zn substrate (JCPDS No. 87−0713) can be readily indexed to a pure *fcc*-

dx.doi.org/10.1021/ic5014126 | Inorg. Chem. 2014, 53, 12289−12296

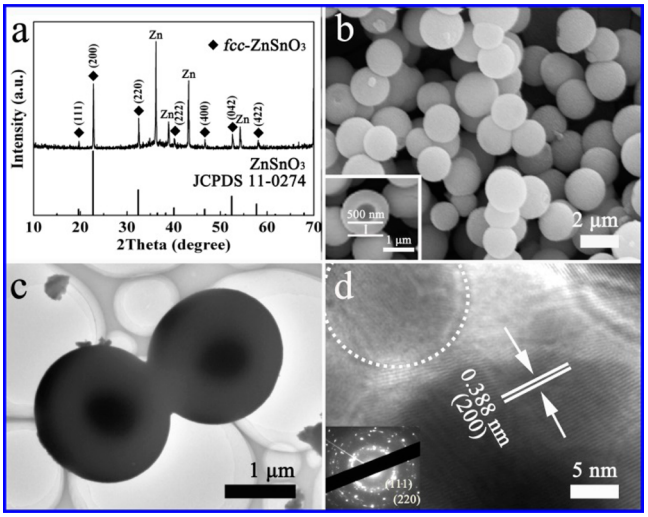

Figure 2. Structure and size of the $ZnSnO_3$ HMs: (a) XRD pattern, (b) SEM image, (c) TEM image, and (d) HRTEM image. The insets of (b) and (d) are typical enlarged SEM image and SAED pattern of $ZnSnO_3$ HMs, respectively.

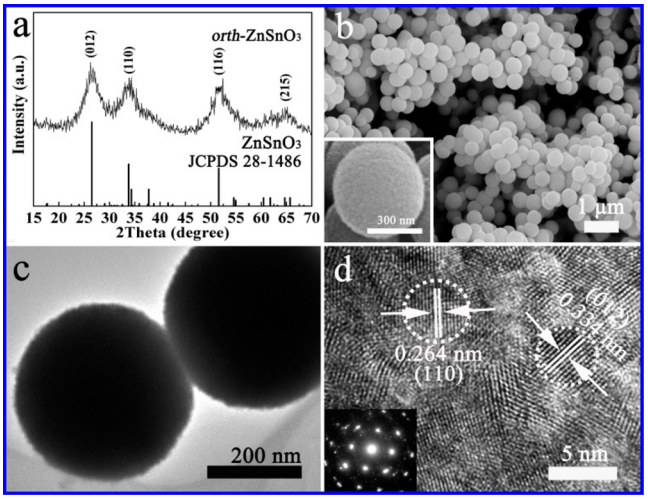

Figure 3. Typical (a) XRD pattern and (b) SEM image, (c) TEM image, (d) high-magnification TEM; the insets of (b) and (d) are typical enlarged SEM image and SAED pattern of $ZnSnO_3$ SMs, respectively.

phase $ZnSnO_3$ with the lattice constants a = 7.768 Å, which is in good agreement with the literature result (JCPDS No. 11−0274). The sample's average crystallite size is ∼16 nm calculated by the Scherrer equation according to the XRD results. No peak from other impurities, such as ZnO and other phase $ZnSnO_3$, etc., is detected, indicating that the products formed on the Zn substrate are pure *fcc*-$ZnSnO_3$.

Furthermore, the morphologies and microstructures of the typical as-prepared $ZnSnO_3$ samples are identified by SEM, TEM, and HRTEM measurements. The panoramic SEM morphology is shown in Figure 2b, which demonstrates that the product growing on the Zn substrate is composed of mass microspheres. The microspheres have smooth surfaces and an average outside diameter of 2 μm. Every microsphere has a hollow interior, and its shell is ∼500 nm thick, as shown in Figure 2b inset and Figure 2c. The product's microstructure, shape, and crystallinity are further confirmed by HRTEM and SAED examinations. From Figure 2d it can be seen that the shell of *fcc*-$ZnSnO_3$ hollow microsphere (HM) is composed of many nanoparticles with ∼15 nm size, as shown in circle sections, and the clear interplanar spacing of a $ZnSnO_3$ HM is 3.88 Å, which corresponds to (200) plane of *fcc*-$ZnSnO_3$. The SAED pattern (inset in Figure 2d) exhibits two intensively bright homocentric rings, which are in good agreement with the (111) and (220) planes of *fcc*-$ZnSnO_3$, indicating the HM's polycrystalline nature. All the above results demonstrate that *fcc*-$ZnSnO_3$ HMs with uniform size and good crystallinity were obtained using ZnO particles as the inducing template and the precursor.

Structural and Morphological Characteristics of *orth*-$ZnSnO_3$ Solid Microspheres in the Solution. The structure and crystalline state of the precipitates formed synchronously in solution are characterized first by XRD measurements, as shown in Figure 3a. All of the diffraction peaks are indexed well to *orth*-$ZnSnO_3$ (JCPDS No. 28−1486) with the lattice constants: a = 3.681 Å, b = 3.804 Å, and c = 14.272 Å. And the sample's average crystallite size is ∼4.3 nm calculated by the Scherrer equation according to the XRD results. No peaks from other impurities, such as ZnO and *fcc*-$ZnSnO_3$, etc., are found, which indicates a high purity of the final *orth*-$ZnSnO_3$.

The sizes, morphologies, and microstructures of the as-prepared samples are further characterized by SEM, TEM, and HRTEM measurements. A typical SEM image in Figure 3b shows that the as-prepared *orth*-$ZnSnO_3$ product consists of a large scale of microspheres with high dispersivity and nearly uniform size: ∼500 nm. And the SEM result of the surface of an individual $ZnSnO_3$ microsphere, as shown in Figure 3b inset, indicates that the microsphere is composed of a large amount of small particles. Its typical TEM and HRTEM images, as shown in Figure 3c,d, further depict the sphere-like morphology and porous microstructure of the *orth*-$ZnSnO_3$ solid microspheres (SMs). The HRTEM image taken from a typical $ZnSnO_3$ SMs demonstrates that the *orth*-$ZnSnO_3$ microsphere is composed of many tiny nanoparticles with ∼4.2 nm size, as shown in circle sections of Figure 3d, which agrees with the calculated size (∼4.3 nm) from the XRD pattern. Mainly, two sets of lattice spacings of 2.64 and 3.37 Å are observed, which correspond to (110) and (012) planes of *orth*-$ZnSnO_3$, respectively. The inset in Figure 3d shows the SAED pattern of a $ZnSnO_3$ SM, indicating its polycrystalline nature, which further confirms the above HRTEM's observation. It has been proved that particle size and porous structure are critical to enhance the gas-sensing property of $ZnSnO_3$.[35,40] So on the basis of the above examination results regarding the *fcc*-$ZnSnO_3$ and *orth*-$ZnSnO_3$, there is reason to believe that the $ZnSnO_3$ products obtained by us may possess remarkable gas-sensitive properties, which has been demonstrated practically by the following corresponding research in this work.

Individual Growth Mechanism of *orth*-$ZnSnO_3$ SMs and *fcc*-$ZnSnO_3$ HMs. To demonstrate the formation process and the individual growth mechanism of *orth*-$ZnSnO_3$ SMs and *fcc*-$ZnSnO_3$ HMs, detailed time-dependent experiments are carried out. Figure 4 shows the SEM images of the *orth*-$ZnSnO_3$ product in solution and the *fcc*-$ZnSnO_3$ product on the Zn substrate collected under different reaction times of 0.5, 3, 10, and 24 h. It is found that sphere-like particles form in a short reaction time (0.5 h), and the particles become uniform (∼500 nm) after a 3 h reaction. As the reaction time is prolonged to 10 or 24 h, as shown in Figure 4c,d, all the as-obtained $ZnSnO_3$ products are still regular, and their diameters increase to 700 and 800 nm, respectively. From the above

dx.doi.org/10.1021/ic5014126 | *Inorg. Chem.* 2014, 53, 12289−12296

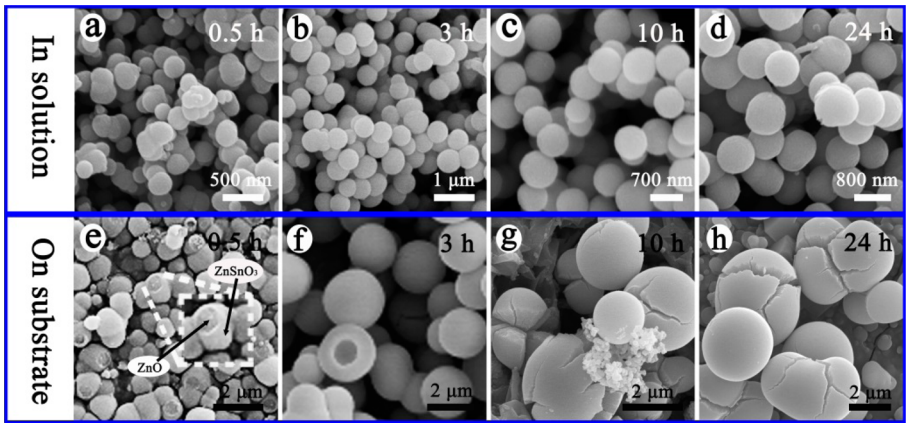

Figure 4. SEM images of morphology evolution of the *orth*-$ZnSnO_3$ SMs in solution and *fcc*-$ZnSnO_3$ HMs on substrate with reaction times: (a), (e) 0.5 h; (b), (f) 3 h; (c), (g) 10 h; and (d), (h) 24 h.

$ZnSnO_3$ products' XRD results (Supporting Information, Figure S3a), it can be seen that all the diffraction peaks are indexed well to *orth*-$ZnSnO_3$ (JCPDS No. 28−1486), and no phase change occurs. Simultaneously, *fcc*-$ZnSnO_3$ forms gradually on ZnO microspherical surfaces on the Zn foil, as shown in Figure 4e and their corresponding XRD patterns (Supporting Information, Figure S3d). As a reactant, ZnO reacts with OH^- and K_2SnO_3 to form $ZnSnO_3$ on its surface first. And then, as the reaction proceeds, more as-formed $ZnSnO_3$ particles cover the whole ZnO surface. Finally a $ZnSnO_3$ shell on ZnO forms, which is also in favor of lowering the total surface energy of the reaction system. After 3 h, the ZnO template is consumed completely, and *fcc*-$ZnSnO_3$ HM is obtained. With the reaction time extending more than 10 h, the $ZnSnO_3$ HMs grow bigger through a recrystalline process and finally are ruptured due to the deficient reactants in the solution and the pressure difference between the interiors of the spheres and external solution.[41] When the reaction time is 3 h, every HM shell is ∼500 nm thick with porous structure, which contains many channels for exchanging between its internal solution in the sphere and the external reaction solution. Then the pressure between the sphere's interior and the external solution keeps balance. As the reaction time is prolonged, the sphere's shell becomes compacted with the aggregation of more new nanoparticles to land on it. And the nanoparticles block the channels, and the pressure balance is broken. With the reduction of the reactant concentrations proceeding in the sphere's interior, the internal solution density is reduced, and its pressure becomes small. So after some time the pressure difference between the sphere's interior and the external solution induces the rupture of the sphere.

Obviously, in this individual growth process ZnO microsphere acts as an inducing template for the formation of $ZnSnO_3$ HM, as shown in Scheme 1. By observing the TEM result (Figure 2c) of *fcc*-$ZnSnO_3$ HMs, it is found that many (200) planes are exposed in the product, and a possible lattice matching relationship between the *fcc*-$ZnSnO_3$ HMs (200) plane and ZnO (100) plane has been illustrated in Scheme 2. And in this process the ZnO structural host motifs react easily with OH^- and K_2SnO_3 with slight lattice rotation and rearrangement of crystal structure, resulting in the favorable matching structures for *fcc*-$ZnSnO_3$. In contrast, when the foil covered with ZnO microspheres is immersed into the reaction solution, some tiny ZnO nanoparticles fall from the substrate and then are dispersed in the solution, which has been proved

Scheme 1. Possible Mechanism Shows the Growth of the *orth*-$ZnSnO_3$ SMs and *fcc*-$ZnSnO_3$ HMs

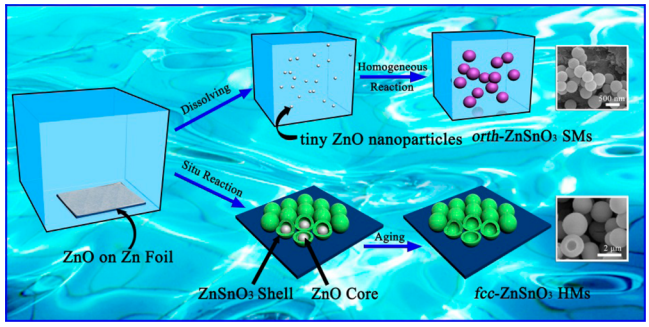

Scheme 2. Schematic Diagram of the Lattice Matching Relationship between ZnO and *fcc*-$ZnSnO_3$

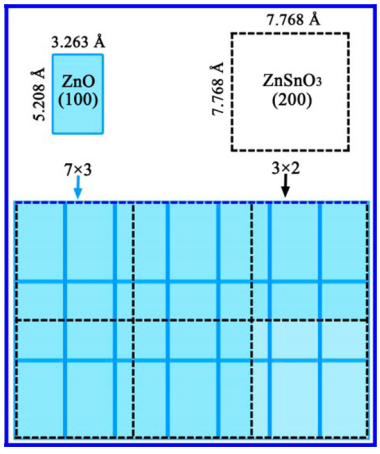

by the corresponding UV−vis absorption spectra examination of the solution reacted for 10 min, as shown in Supporting Information, Figure S4, where the UV-absorption peak of ZnO at 372 nm and UV-absorption peak of $ZnSnO_3$ at ∼500 nm can be clearly seen, and these values are in good agreement with those found in the literature,[42,43] which confirms the existence of ZnO tiny nanoparticles in the solution. After that, tiny $ZnSnO_3$ nanoparticles continuously aggregate and nucleate based on *orth*-$ZnSnO_3$ cell structure. The growth of *orth*-$ZnSnO_3$ in solution is a very small-level reaction, in which the final product is mainly determined by the nucleation process.

dx.doi.org/10.1021/ic5014126 | *Inorg. Chem.* 2014, 53, 12289−12296

Table 1. Comparation of Gas Responses of $ZnSnO_3$ Sensors to Ethanol Gas in This Work and Those Reported in Literature

	response			time	
morphology (crystal phase, size)	S^a	C^b (ppm)	T^c (°C)	R^d (s)	R^e (s)
nanocages[44] (*fcc*, 20 nm)	30	200	270	<2	30
microspheres[45] (*fcc*, 7 nm)	110	500	275	3	30
HMs (this work) (*fcc*, 16 nm)	144.3	500	320	7	8
nanowires[46] (*orth*, 60 nm)	42	500	300	1	1
nanorods[35] (*orth*, 45 nm)	50	400	300	<10	<10
SMs (this work) (*orth*, 4.3 nm)	80	500	260	4	7
nanorods[34] (*orth*, 3 nm)	109	500	250	5	15
nanosheets[40] (*orth*, 15−20 nm)	135	500	320	0.36	9

[a]S: sensitivity. [b]C: concentration. [c]T: temperature. [d]R: response. [e]R: recovery.

The formation process of the two products can be described by eqs 1−3.

$$CO(NH_2)_2 + H_2O \rightarrow NH_4^+ + OH^- + CO_2 \quad (1)$$

$$K_2SnO_3 + ZnO(l) + OH^- \rightarrow orth\text{-}ZnSnO_3 + KOH + H_2O \quad (2)$$

$$K_2SnO_3 + ZnO(s) + OH^- \rightarrow fcc\text{-}ZnSnO_3 + KOH + H_2O \quad (3)$$

Usually reaction temperature and reactant concentration are the most direct influencing factors on the kinetics and thermodynamics process in material synthesis. Therefore, to clarify the contribution of kinetic/thermodynamic parameters in the *orth*-$ZnSnO_3$ and *fcc*-$ZnSnO_3$ growth processes, additional experiments with different reaction temperatures, additional amounts of K_2SnO_3 and urea, and varying reaction times were conducted (Supporting Information, Figure S3). Thermodynamics focuses on researching the driving force of a system moving from an initial state to a final state, while kinetics is concerned with the barriers of the various pathways in this process. For the chemical reactions of different phases, it is important to distinguish whether they are thermodynamically or kinetically controlled. In this work, through detailed experimental study, it is found that pure *orth*-$ZnSnO_3$ products can be obtained just when the reaction temperature is above 100 °C, and neither reactant concentration nor reaction time has obvious effect on the *orth*-$ZnSnO_3$ growth. So the formation of *orth*-$ZnSnO_3$ is mainly controlled by thermodynamic factors. As for the formation of *fcc*-$ZnSnO_3$, the reaction time, reaction temperature, and reactant concentration are all the crucial factors to the purities and crystal structures of the final products. Therefore, the growth process of *fcc*-$ZnSnO_3$ sample is affected by both thermodynamic parameter and kinetic parameter. In addition, the morphology evolution of *orth*-$ZnSnO_3$ SMs and *fcc*-$ZnSnO_3$ HMs under different reaction temperatures, K_2SnO_3 concentrations, and ZnO precursors were also studied (Supporting Information, Figure S5).

Gas-Sensing Properties of the Products. Recently, $ZnSnO_3$ has been demonstrated as a new type of excellent gas-sensitive material for detecting reducing and combustible gases, especially ethanol gas, as listed in Table 1. On the basis of the literature values listed in Table 1, three rules can be concluded: (1) Without regard to size and morphology, *fcc*-$ZnSnO_3$ represents the higher sensitivity than *orth*-$ZnSnO_3$.[44−46] (2) The hollow structures show better response compared with the solid ones due to their larger surface/volume ratios.[35,40,46] (3) As the grain size is comparable to the Debye length (tens of nanometers for metal oxides in general), the material's surface activity is increased greatly, and the smaller size often results in higher sensitivity.[34,35,44−46] On the basis of the above rules, it is reasonable to believe that the as-obtained *fcc*-$ZnSnO_3$ product with hollow structure and small crystal size (∼16 nm) in this work may exhibit exciting gas-sensing properties, which is demonstrated factually by the following experiments.

The BET surface area of the $ZnSnO_3$ SMs and $ZnSnO_3$ HMs were investigated by N_2 adsorption−desorption measurements (Supporting Information, Figure S6). The surface area of $ZnSnO_3$ HMs is ∼62.5096 $m^2\ g^{-1}$. The BET nitrogen adsorption−desorption analysis of the $ZnSnO_3$ SMs has also been measured. It represents a surface area of 40.4383 $m^2\ g^{-1}$. To our knowledge, a larger surface/volume ratio is able to effectively improve the gas-sensing performance.[47,48] On the basis of the results above, we investigated the gas-sensing characteristics of $ZnSnO_3$ HMs and $ZnSnO_3$ SMs. Moreover, the gas-sensing properties of the composite of $ZnSnO_3$ shell−ZnO core were also analyzed as shown in detail in Supporting Information, Figure S7.

The sensors based on the as-synthesized $ZnSnO_3$ SMs and $ZnSnO_3$ HMs are fabricated and tested using a method similar to the previous report.[34] The optimal operating temperatures of the $ZnSnO_3$ SMs and $ZnSnO_3$ HMs sensors for detecting ethanol are investigated first. Figure 5a shows the sensitivities of the two products to 500 ppm ethanol under different working temperatures. It is found that most optimum working tempeatures of them are 260 °C (for $ZnSnO_3$ SMs) and 320 °C (for $ZnSnO_3$ HMs), which are comparable with the literature values.

Figure 5b shows the time-dependent sensitivity of the sensors toward 10−500 ppm ethanol at the optimal operating temperatures of 320 °C ($ZnSnO_3$ HMs) and 260 °C ($ZnSnO_3$ SMs). It is found that the sensitivity of the sensor based on $ZnSnO_3$ HMs increases rapidly with the increase of ethanol concentration, and it reaches 144.3 for 500 ppm ethanol, which is much higher than that of other *fcc*-$ZnSnO_3$ nanoparticles. Under 10−500 ppm ethanol, the response and recovery time of both $ZnSnO_3$ SMs and $ZnSnO_3$ HMs are less than 10 s, indicating their good sensitivities. Though many cycles between the ethanol vapor and fresh air are conducted, the responses of the sensors still maintain their high level, which implies that the sensors have good reversibility and stability. Figure 5c shows the sensitivity of the sensors as a function of ethanol concentration. It is found that the S values of sensitivity for $ZnSnO_3$ HMs increase rapidly with ethanol concentrations upward. However, the S value of $ZnSnO_3$ SMs increases slowly with the adding of ethanol concentration. This suggests that

dx.doi.org/10.1021/ic5014126 | Inorg. Chem. 2014, 53, 12289−12296

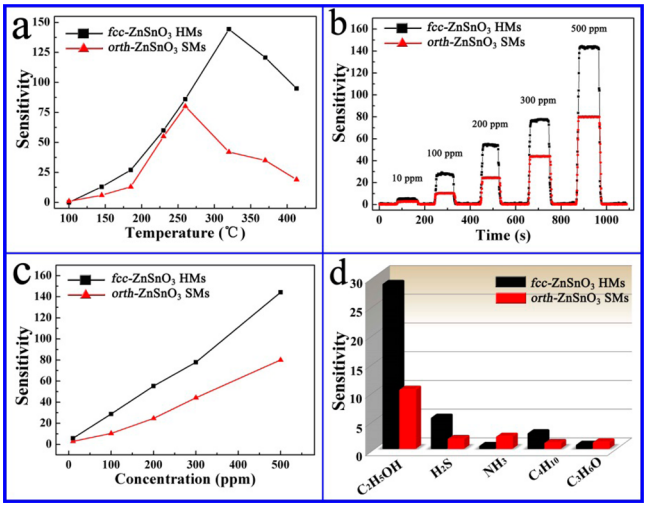

Figure 5. (a) The sensitivities of *fcc*-$ZnSnO_3$ HMs and *orth*-$ZnSnO_3$ SMs to 500 ppm of C_2H_5OH as a function of operating temperature. The sensitivity of the sensors based on the final products to the tested gases at 320 °C ($ZnSnO_3$ HMs) and 260 °C ($ZnSnO_3$ SMs): (b) the time-dependent sensitivity of the sensors toward 10−500 ppm ethanol; (c) the sensitivity of $ZnSnO_3$ HMs and $ZnSnO_3$ SMs as a function of ethanol concentration. (d) The *S* value of $ZnSnO_3$ HMs and $ZnSnO_3$ SMs sensors to various test gases of 100 ppm.

compared with $ZnSnO_3$ SMs, $ZnSnO_3$ HMs are more favorable in detecting ethanol vapor in a wide ethanol concentration range.

Compared with previous reports about ethanol-sensing properties of $ZnSnO_3$-based gas sensors, the products (both $ZnSnO_3$ SMs and $ZnSnO_3$ HMs) in the present work exhibit significantly improved sensing abilities, as listed in Table 1 characteristics. For instance, the optimum operating temperature of *orth*-$ZnSnO_3$ SMs in this work decreased from more than 300 °C (*orth*-$ZnSnO_3$ hollow fibers[35] and *orth*-$ZnSnO_3$ sheets[40]) to 260 °C; compared with the sensitivity of the *fcc*-$ZnSnO_3$ nanocage sensors (500 ppm ethanol gas, S = 32.0), a much higher sensitivity (500 ppm ethanol gas, S = 144.3) is reached for the *fcc*-$ZnSnO_3$ HMs in this work. For an individual metal oxide nanostructure, the space-charge layer (its width, L_d), which is ∼tens of nanometers in general, would be fabricated at the surface owing to the electrons extracted from the bulk by adsorbed oxygen ions. When the size of the sensing materials is close to 2 L_d, all electrons will be almost fully depleted.[40,49] Thus, the *fcc*-$ZnSnO_3$ HMs and *orth*-$ZnSnO_3$ SMs with tiny nanograins of 16 and 4.3 nm have significantly improved sensing properties.[34] It has been proved that the grain size and morphology of $ZnSnO_3$ materials are the critical effect factors to their gas-sensing properties.[50−53] Furthermore, we also investigated the effect of crystallinity and found that the crystallinity does not affect the gas-sensing properties of *fcc*-$ZnSnO_3$ HMs and *orth*-$ZnSnO_3$ SMs (see Supporting Information, Figure S8). Simultaneously, the two sensors fabricated by the *fcc*-$ZnSnO_3$ HMs and *orth*-$ZnSnO_3$ SMs represent good selectivity to ethanol gas. As shown in Figure 5d, the responses of *fcc*-$ZnSnO_3$ HM and *orth*-$ZnSnO_3$ SM sensors to 100 ppm of H_2S, NH_3, C_4H_{10}, and C_3H_6O are measured at 320 and 260 °C, respectively, in which it is found that the sensors' responses to H_2S, NH_3, C_4H_{10}, and C_3H_6O are much less than that for ethanol vapor. As we know that the acid−base properties of a basic oxide are found to have enhanced sensing characteristics for a complex molecular structure or a reactive functional group such as ethanol,[54] the sensors based on $ZnSnO_3$ SMs and $ZnSnO_3$ HMs show obvious advantage in selective detection of ethanol in this work.

$ZnSnO_3$ is well-known as an n-type semiconductor, characterized by its high free carrier concentration. Exposure of the $ZnSnO_3$ sensors to air results in O_2 adsorption on its surface to form chemisorbed oxygen species (O_2^-, O^{2-}, O^-) due to the strong electronegativity of the oxygen atom. Therefore, the electrical conductivity of $ZnSnO_3$ sensor depends strongly on the surface states produced by molecular adsorption, which results in an electron depletion layer at the surface of the materials.[55,56] When a reductive gas, such as ethanol, is introduced, a chemical reaction takes place between ethanol and the adsorbed oxygen, which results in a relatively strong activation on the surface of the $ZnSnO_3$ sensor.[57,58] Ethanol vapor decomposes to CH_3CHO and finally to CO_2 and H_2O as follows:

$$C_2H_5OH_{(ads)} + O^-_{(ads)} \rightarrow CH_3CHO_{(ads)} + H_2O_{(ads)} + e^- \quad (4)$$

$$CH_3CHO_{(ads)} + 5O^-_{(ads)} \rightarrow 2CO_2 + 2H_2O + 5e^- \quad (5)$$

In this process, electrons are released, and the electron concentration in $ZnSnO_3$ material increases, resulting in its resistance decreasing.[59] Furthermore, typical photoluminescence (PL) spectra examinations and resistivity measurements of the *orth*-$ZnSnO_3$ SMs and *fcc*-$ZnSnO_3$ HMs were conducted and analyzed to evaluate their defect state, especially their oxygen vacancy concentrations. The room-temperature PL spectrum (Supporting Information, Figure S9) shows that both of the *orth*-$ZnSnO_3$ SMs and *fcc*-$ZnSnO_3$ HMs show a similar strong blue emission peak at ∼461 nm under 270 nm UV excitation, and the intensity of the *fcc*-$ZnSnO_3$ HMs peak is higher than that of the *orth*-$ZnSnO_3$ SMs. This emission peak of $ZnSnO_3$ material is due to the existence of oxygen vacancies.[60] In addition, the bigger peak intensity indicates that the oxygen vacancy concentration of *fcc*-$ZnSnO_3$ HMs is higher than that of *orth*-$ZnSnO_3$ SMs in the equal quality.[61] It is known that in metal oxides the more oxygen vacancies exist, the lower the resistivity.[62] In this work, the low resistivities of *orth*-$ZnSnO_3$ SMs and *fcc*-$ZnSnO_3$ HMs are 2.70×10^{-2} Ω cm and 1.05×10^{-2} Ω cm, respectively, at room temperature, which are lower than the literature values,[63] indicating the higher concentrations of oxygen vacancies in the as-obtained samples. And the resistivity of *fcc*-$ZnSnO_3$ HMs is lower than that of the *orth*-$ZnSnO_3$ SMs, which agrees with the results of PL spectrum examinations. High level of oxygen vacancy is of benefit to the electrostatic interaction between the gas molecules (such as ethanol molecules) and $ZnSnO_3$ sensor,[60] and in addition, it also greatly increases the surface activities and remarkably decreases their optimum working temperature in gas-sensing process. So the $ZnSnO_3$ materials prepared in this work, especially the *fcc*-$ZnSnO_3$ HMs, display low resistivity and high oxygen vacancy concentrations, resulting in the enhanced ethanol gas-sensing properties at a relatively low working temperature. In addition, in this work, the as-obtained $ZnSnO_3$ SMs and $ZnSnO_3$ HMs are composed of tiny nanoparticles and display porous structures, which favor the electron transferring with a higher rate and provide larger surface area for gas adsorption and diffusion.[64,65] This also leads to further enhancement in their gas sensitivities.

dx.doi.org/10.1021/ic5014126 | *Inorg. Chem.* 2014, 53, 12289−12296

CONCLUSIONS

In summary, a template-inducing method has been applied to intervene against the $ZnSnO_3$ allotrope blending, in which the isolated allotropes (*fcc*- and *orth*-$ZnSnO_3$) are located in the appointed regions in the same reaction system. And the growing mechanisms based on the different nucleation and growth process of the $ZnSnO_3$ allotropes have also been demonstrated, which put forward the step toward the realization of allotropes dividing. In addition, both the gas sensors based on *orth*-$ZnSnO_3$ SMs and *fcc*-$ZnSnO_3$ HMs showed themselves to be highly sensitive to ethanol with fast response and recovery and good selectivity and stability due to their tiny particle sizes and porous structures. The following work on validating the feasibility of this method for other allotropes dividing is now on the way.

ASSOCIATED CONTENT

Supporting Information

The detail of $ZnSnO_3$ allotropes particles, as-prepared ZnO, as-prepared *orth*-$ZnSnO_3$ SMs and *fcc*-$ZnSnO_3$ HMs under different reaction conditions, the sensitivity of $ZnSnO_3$ shell−ZnO core microspheres, and BET measurement. This material is available free of charge via the Internet at http://pubs.acs.org.

AUTHOR INFORMATION

Corresponding Authors

*gaopeng@hrbeu.edu.cn. (P.G.)
*chenyujin@hrbeu.edu.cn. (Y.C.)
*yangpiaoping@hrbeu.edu.cn. (P.Y.)

Author Contributions

The manuscript was written through contributions of all authors. All authors have given approval to the final version of the manuscript. All authors contributed equally.

Notes

The authors declare no competing financial interest.

ACKNOWLEDGMENTS

We thank the Program for NCET in University (NCET-10-0049, NCET-13-0754), the Natural Science Foundation of China (Grant No. 51272050 and 51072038); the Specialized Research Fund for the Doctoral Program of Higher Education of China (No. 20092304120021); Harbin Sci-Tech Innovation Foundation (RC2012XK017012); Harbin Key Sci-Tech (Project No. 2010AA4BG004); the Fundamental Research funds for the Central Universities (No. HEUCF201403007), and Outstanding Youth Foundation of Heilongjiang Province (Grant No. JC201008) for the financial support of this research.

ABBREVIATIONS

orth, orthorhombic
fcc, face-centered cubic
SM, solid microsphere
HM, hollow microsphere

REFERENCES

(1) Yu, L. *J. Am. Chem. Soc.* **2003**, *125*, 6380−6381.
(2) Bernstein, J.; Davey, R. J.; Henck, J. O. *Angew. Chem., Int. Ed.* **1999**, *38*, 3440−3461.
(3) Moreo, A.; Yunoki, S.; Dagotto, E. *Science* **1999**, *283*, 2034−2040.
(4) Liu, Z. Y.; Zhang, X. T.; Nishimoto, S.; Jin, M.; Tryk, D. A.; Murakami, T.; Fujishima, A. *Langmuir* **2007**, *23*, 10916−10919.
(5) Vasudevan, R. K.; Liu, Y. Y.; Li, J. Y.; Liang, W.; Kumar, A.; Jesse, S.; Chen, Y. C.; Chu, Y. H.; Nagarajan, V.; Kalinin, S. V. *Nano Lett.* **2011**, *11*, 3346−3354.
(6) Kanamori, K.; Nakanishi, K.; Hanada, T. *Adv. Mater.* **2006**, *18*, 2407−2411.
(7) Seo, M.; Hillmyer, M. A. *Science* **2012**, *336*, 1422−1425.
(8) Jung, Y.; Lee, S. H.; Jennings, A. T.; Agarwal, R. *Nano Lett.* **2008**, *8*, 2056−2062.
(9) Zhang, S. X.; Kim, I. S.; Lauhon, L. J. *Nano Lett.* **2011**, *11*, 1443−1447.
(10) Shin, S. J.; Guzman, J.; Yuan, C. W.; Liao, C. Y.; Boswell-Koller, C. N.; Stone, P. R.; Dubon, O. D.; Minor, A. M.; Watanabe, M.; Beeman, J. W.; Yu, K. M.; Ager, J. W., III; Chrzan, D. C.; Haller, E. E. *Nano Lett.* **2010**, *10*, 2794−2798.
(11) Jung, Y.; Yang, C. Y.; Lee, S. H.; Agarwa, R. *Nano Lett.* **2009**, *9*, 2103−2108.
(12) Dermatas, D.; Chrysochoou, M.; Moon, D. H.; Grubb, D. G.; Wazne, M.; Christodoulatos, C. *Environ. Sci. Technol.* **2006**, *40*, 5786−5792.
(13) Mott, N. F. *Rev. Mod. Phys.* **1968**, *40*, 677−683.
(14) Vanitha, P. V.; O'Brien, P. *J. Am. Chem. Soc.* **2008**, *130*, 17256−17257.
(15) Kawahara, T.; Ozawa, T.; Iwasaki, M.; Tada, H.; Ito, S. *J. Colloid Interface Sci.* **2003**, *267*, 377−381.
(16) Morgan, B. J.; Madden, P. A. *Nano Lett.* **2004**, *4*, 1581−1585.
(17) Gilman, H.; Jokesz, R. G.; Woods, L. A. *J. Org. Chem.* **1952**, *17*, 1630−1634.
(18) Itkis, M. E.; Perea, D. E.; Niyogi, S.; Rickard, S. M.; Hamon, M. A.; Hu, H.; Zhao, B.; Haddon, R. C. *Nano Lett.* **2003**, *3*, 309−314.
(19) Scrivens, W. A.; Bedworth, P. V.; Tour, J. M. *J. Am. Chem. Soc.* **1992**, *114*, 7917−7919.
(20) Kabalah-Amitai, L.; Mayzel, B.; Kauffmann, Y.; Fitch, A. N.; Bloch, L.; Gilbert, P. U. P. A.; Pokroy, B. *Science* **2013**, *340*, 454−456.
(21) Liu, L. G.; Bassett, W. A.; Liu, M. S. *Science* **1973**, *180*, 298−299.
(22) Piermarini, G. J.; Weir, C. E. *Science* **1964**, *144*, 69−71.
(23) Jin, L. X.; Liu, W. P.; Lin, C. M.; Gan, J. *ACS Symp. Ser.* **2011**, *1085*, 67−79.
(24) Ye, J.; Zhang, Y.; Chen, S. W.; Liu, C. N.; Zhu, Y. Q. *Aquat. Toxicol.* **2014**, *146*, 12−19.
(25) Lamer, V. K.; Dinega, R. H. *J. Am. Chem. Soc.* **1950**, *72*, 4847−4854.
(26) Zhu, C.; Zeng, J.; Lu, P.; Liu, J. Y.; Gu, Z. Z.; Xia, Y. N. *Chem.—Eur. J.* **2013**, *19*, 5127−5133.
(27) Wang, H. Q.; Nann, T. *ACS Nano* **2009**, *3*, 3804−3808.
(28) Mao, C. B.; Solis, D. J.; Reiss, B. D.; Kottmann, S. T.; Sweeney, R. Y.; Hayhurst, A.; Georgiou, G.; Iverson, B.; Belcher, A. M. *Science* **2004**, *303*, 213−217.
(29) Jin, C.; McLachlan, M. A.; McComb, D. W.; De La Rue, R. M.; Johnson, N. P. *Nano Lett.* **2005**, *5*, 2646−2650.
(30) Gierszal, K. P.; Jaroniec, M. *J. Am. Chem. Soc.* **2006**, *128*, 10026−10027.
(31) Bhattacharya, S.; Stojakovi, J.; Saha, B. K.; MacGillivray, L. R. *Org. Lett.* **2013**, *15*, 744−747.
(32) Tian, Z. R.; Voigt, J. A.; Liu, J.; Mckenzie, B.; Xu, H. F. *J. Am. Chem. Soc.* **2003**, *125*, 12384−12385.
(33) Aizenberg, J.; Muller, D. A.; Grazul, J. L.; Hamann, D. R. *Science* **2003**, *299*, 1205−1208.
(34) Men, H.; Gao, P.; Zhou, B. B.; Chen, Y. J.; Zhu, C. L.; Xiao, G.; Wang, L. Q.; Zhang, M. L. *Chem. Commun.* **2010**, *46*, 7581−7583.
(35) Song, P.; Wang, Q.; Yang, Z. X. *Sens. Actuators, B* **2011**, *156*, 983−989.
(36) Kovacheva, D.; Petrov, K. *Solid State Ionics* **1998**, *109*, 327−332.
(37) Yim, K. H.; Doherty, W. J.; Salaneck, W. R.; Murphy, C. E.; Friend, R. H.; Kim, J. S. *Nano Lett.* **2010**, *10*, 385−392.
(38) Chen, Y. J.; Zhu, C. L.; Xiao, G. *Sens. Actuators, B* **2008**, *129*, 639−642.
(39) Chen, Y. J.; Zhu, C. L.; Xiao, G. *Nanotechnology* **2006**, *17*, 4537−4541.

(40) Chen, Y. J.; Yu, L.; Li, Q.; Wu, Y.; Li, Q. H.; Wang, T. H. *Nanotechnology* **2012**, *23*, 415501.
(41) Geng, B. Y.; You, J. H.; Zhan, F. M.; Kong, M. G.; Fang, C. H. *J. Phys. Chem. C* **2008**, *112*, 11301−11306.
(42) Liu, B.; Zeng, H. C. *J. Am. Chem. Soc.* **2004**, *126*, 16744−16746.
(43) Chu, X. F.; He, Y. Q.; Li, Y. M.; Huang, H. Z.; Liu, D. Y.; Chen, H. M.; Li, W. Y. *Chin. J. Inorg. Chem.* **2014**, *30*, 1212−1220.
(44) Zeng, Y.; Zhang, T.; Fan, H. T.; Fu, W. Y.; Lu, G. Y.; Sui, Y. M.; Yang, H. B. *J. Phys. Chem. C* **2009**, *113*, 19000−19004.
(45) Sun, P.; Sun, Y. F.; Ma, J.; You, L.; Lu, G. Y.; Fu, W. Y.; Li, M. H.; Yang, H. B. *Sens. Actuators, B* **2011**, *155*, 606−611.
(46) Xue, X. Y.; Chen, Y. J.; Wang, Y. G.; Wang, T. H. *Appl. Phys. Lett.* **2005**, *86*, 233101.
(47) Li, L. L.; Zhang, W. M.; Yuan, Q.; Li, Z. X.; Fang, C. J.; Sun, L. D.; Wan, L. J.; Yan, C. H. *Cryst. Growth Des.* **2008**, *8*, 4165−4172.
(48) Gyger, F.; Hübner, M.; Feldmann, C.; Barsan, N.; Weimar, U. *Chem. Mater.* **2010**, *22*, 4821−4827.
(49) Paulose, M.; Varghese, O. K.; Mor, G. K.; Grimes, C. A.; Ong, K. G. *Nanotechnology* **2006**, *17*, 398−402.
(50) Shen, Y. S.; Zhang, T. S. *Sens. Actuators, B* **1993**, *12*, 5−9.
(51) Geng, B. Y.; Fang, C. H.; Zhan, F. M.; Yu, N. *Small* **2008**, *4*, 1337−1343.
(52) Wang, W. W.; Zhu, Y. J.; Yang, L. X. *Adv. Funct. Mater.* **2007**, *17*, 59−64.
(53) Zeng, Y.; Zhang, T.; Fan, H. T.; Lu, G. Y.; Kang, M. H. *Sens. Actuators, B* **2009**, *143*, 449−453.
(54) Gopal Reddy, C. V.; Cao, W.; Tan, O. K.; Zhu, W. *Sens. Actuators, B* **2002**, *81*, 170−175.
(55) Eranna, G.; Joshi, B. C.; Runthala, D. P.; Gupta, R. P. *Crit. Rev. Solid State Mater. Sci.* **2004**, *29*, 111−188.
(56) Xu, J. Q.; Chen, Y. P.; Chen, D. Y.; Shen, J. N. *Sens. Actuators, B* **2006**, *113*, 526−531.
(57) Chen, Y. J.; Xue, X. Y.; Wang, Y. G.; Wang, T. H. *Appl. Phys. Lett.* **2005**, *87*, 233503.
(58) Song, F.; Su, H. L.; Han, J.; Xu, J. Q.; Zhang, D. *Sens. Actuators, B* **2010**, *145*, 39−45.
(59) Xu, J. Q.; Jia, X. H.; Lou, X. D.; Xi, G. X.; Han, J. J.; Gao, Q. H. *Sens. Actuators, B* **2007**, *120*, 694−699.
(60) Wang, J. X.; Sun, X. W.; Xie, S. S.; Zhou, W. Y.; Yang, Y. *Cryst. Growth Des.* **2009**, *8*, 707−710.
(61) Bao, D.; Gao, P.; Wang, L. Q.; Wang, Y.; Chen, Y. J.; Chen, G. R.; Li, G. B.; Chang, C.; Qin, W. *ChemPlusChem* **2013**, *78*, 1266−1272.
(62) Epifani, M.; Prades, J. D.; Comini, E.; Pellicer, E.; Avella, M.; Siciliano, P.; Faglia, G.; Cirera, A.; Scotti, R.; Morazzoni, F.; Morante, J. R. *J. Phys. Chem. C* **2008**, *112*, 19540−19546.
(63) Kurz, A.; Aegerter, M. A. *Thin Solid Films* **2008**, *516*, 4513−4518.
(64) Cui, Y.; Wei, Q. Q.; Park, H. K.; Lieber, C. M. *Science* **2001**, *293*, 1289−1292.
(65) Shah, R. R.; Abbott, N. L. *Science* **2001**, *293*, 1296−1299.